UWB Beam-Based Local Diffraction Tomography—Part II: The Inverse Problem

Ram Tuvi, Ehud Heyman, *Life Fellow, IEEE*, and Timor Melamed, *Senior Member, IEEE*

***Abstract*— This two-part article is concerned with the medium reconstruction using the beam-based tomographic inverse scattering. This Part II is based on the results of Part I that has dealt with the preprocessing phase. Specifically, we defined there the beam-frame representation of the scattered field and the corresponding processing windows that transform the scattering data to the beam domain. We have also derived the "local time-domain diffraction tomography" relation according to which the beam-domain data are directly related to the local Radon transform (LRT) of the medium. This local transform can be inverted and is used here for the local reconstruction of the medium via beam-domain filtered backpropagation. In this article, we define the filtered backpropagated beam waves and then reconstruct the medium in any sub-domain of interest (DoI) by aggregating the contributions of the backpropagated beams that pass in or near that DoI. Specifically, we use the class of isodiffracting beam waves, namely, the isodiffracting Gaussian beams (ID-GBs) and the isodiffracting pulse beams (ID-PBs) for the frequency- and time-domain formulations, respectively. Explicit expressions for the filtered backpropagated reconstruction kernels are given. The efficacy of the beam-domain approach for local backpropagation and reconstruction is demonstrated via numerical examples of the synthetic noisy data.**

***Index Terms*— Beam summation methods, diffraction tomography (DT), inverse scattering.**

NOMENCLATURE

UWB	Ultrawideband.
GB	Gaussian beam.
PB	Pulsed beam.
ID	Isodiffracting.
FD	Frequency domain.
TD	Time domain.
WFT	Windowed Fourier transform.
WRT	Windowed Radon transform.
LRT	Local Radon transform.
SST	Slant stack transform.
BF	Beam frame.
PBF	Pulsed-beam frame.
DT	Diffraction tomography.

Manuscript received December 15, 2018; revised November 27, 2019; accepted April 25, 2020. Date of publication May 12, 2020; date of current version October 6, 2020. This work was supported in part by the Israeli Science Foundation (ISF) under Grant 412/15 and Grant 1111/19. *(Corresponding author: Ehud Heyman.)*

Ram Tuvi was with the School of Electrical Engineering, Tel Aviv University, Tel Aviv 69978, Israel. He is now with the Jackson School of Geosciences, Institute for Geophysics, The University of Texas at Austin, Austin, TX 78758 USA (e-mail: ram.tuvi@gmail.com).

Ehud Heyman is with the School of Electrical Engineering, Tel Aviv University, Tel Aviv 69978, Israel (e-mail: heyman@tau.ac.il).

Timor Melamed is with the School of Electrical and Computer Engineering, Ben-Gurion University of the Negev, Be'er Sheva 8410501, Israel (e-mail: timormel@bgu.ac.il).

Color versions of one or more of the figures in this article are available online at http://ieeexplore.ieee.org.

Digital Object Identifier 10.1109/TAP.2020.2992835

I. INTRODUCTION

AS DISCUSSED in the extensive introduction of Part I of this article [1], this Part II is concerned with a beam-based approach for UWB tomographic inverse scattering. We present two inversion schemes— an FD scheme and a TD scheme—which are used, respectively, when the data are expressed over a wide frequency band or in the TD. We, therefore, use the generic term "beams" for both the FD and the TD schemes, where the beam-propagators and the resulting processing windows are based on the isodiffracting Gaussian beams (ID-GBs) and the isodiffracting pulsed beams (ID-PBs), respectively.

Part I of this article has dealt with the forward and the preprocessing problems. We defined the BF representation of the scattered field and then the corresponding processing windows that transform the scattering data to the "beam-domain data," which is the set of beam-amplitudes $\hat{A}_{\boldsymbol{\mu}}$ in (§§17) and $A_{\boldsymbol{\mu},s}$ in (§§24)[1] that describe the scattered field in the FD or TD, respectively.[2] As discussed after these equations, these operations may be regarded, quite simplistically, as WFT or WRT of the FD or TD data, respectively. However, since they are not structured upon a Cartesian phase space lattice, but rather upon the beam lattice, we refer to them as the "BF transform" and the "PBF transform," respectively.

Utilizing the Born approximation, we then derived analytic expressions for $A_{\boldsymbol{\mu},s}$ and demonstrated that they are directly related to local projections of the medium function onto space–time windows that are formed by the PB propagators as they traverse through the medium (see (§§26) and Fig. §§6). This operation, termed there LRT of the medium,[3] extracts the local stratification of the medium and, thus, has a cogent physical interpretation as a local generalized Snell's law. This basic relation between the medium and the beam-domain data provides the basis for the "local TD DT" considered here.

Following this observation, the local reconstruction in this article can be formulated as an inverse LRT, obtained by aggregating the contributions of the beam-scattering amplitudes $A_{\boldsymbol{\mu},s}$ corresponding to the given subdomain of interest (DoI). Following [3], this reconstruction is expressed here as a filtered backpropagation, which is calculated either in the multi-FD (i.e., in a frequency-by-frequency fashion in Section III) or directly in the TD (see Section IV).

[1] We make extensive reference to specific equations, figures, and sections in [1] and [2], denoting them by the prefixes §§ and §, respectively.

[2] As defined in [1], FD constituents are tagged by an over-hat, FD beam constituents are tagged by the phase-space index $\boldsymbol{\mu}$ that defines the beam axis, while TD beam constituents are tagged in addition by the time index s that defines the PB's reference times along these axes

[3] See footnote 3 in Part I [1] of this article for the terminology corresponding to the WRT versus the LRT.

Our main goal in this article is the formulation of the beam-based filtered backpropagation and inverse scattering algorithms within a given DoI. Accordingly, we considered only illuminations from the z_1 plane and measurement of the reflected field within a limited aperture in the same plane. As discussed in Sections §§III-A4 and §§III-B, these data are insufficient for the reconstruction of a general medium, and it is more appropriate for reconstruction of media with strong longitudinal variation and weaker transversal variation. The problems used in the reconstruction examples in Sections V and VI were chosen specifically to model such media, yet they represent a quite complex class of problems that are of interest in many applications. It is worth noting that our method has recently been applied successfully for a realistic seismic inversion in [9].

We start the presentation in Sections II-B and II-C with a short presentation of the UWB filtered backpropagation imaging formulations in the multi-FD and the TD, respectively. For clarity, the derivation of these formulations is deferred to Appendix A. We proceed in Sections III and IV with the beam-domain backpropagation in the multi-FD and the TD, respectively, thus formulating the local inversion schemes. The intricate analytic details of the algorithm as well as its properties are then studied and discussed via the numerical examples in Sections V and VI. The presentation is completed in Section VII with an overall summary and conclusions of Parts I and II.

II. Plane-Wave-Based Backpropagation Imaging

A. Problem Formulation

We consider the reconstruction of a weakly inhomogeneous medium with wave speed $v(\mathbf{r})$ embedded in a uniform medium with wave speed v_0. The unknown medium is identified by the object (or contrast) function $O(\mathbf{r}) = (v_0^2/v^2(\mathbf{r})) - 1$ [see (§§1)]. The interrogation is the pulsed plane-wave $u^i(\mathbf{r}, t)$ in (§§11) that propagates in the $\mathring{\boldsymbol{\kappa}}^i$ direction, and the scattering data $u_j^s(\mathbf{x}, t)$, $j = 1, 2$, are measured on the plane $z = z_1 < 0$ and/or the plane $z = z_2 > 0$, located, respectively, before or after the unknown object O [see Fig. §§1(a)]. Here and henceforth, the index $j = 1, 2$, denote the wave constituents associated with the data u_j, $\mathbf{r} = (\mathbf{x}, z)$ denotes the points in the 3-D coordinate domain with $\mathbf{x} = (x_1, x_2)$ being coordinates transverse to z, and overcircles are used to identify unit vectors.

For weak scatterers, the scattered field is linearly related to the medium via the first-order Born approximation. This relation can be cast in a format, referred to as DT, that directly relates O to the spectrum of the scattered field. In the FD formulations, the DT relation is given in (§§7) and Fig. §§2(b). As discussed in Section §§III-A(4) and illustrated in Fig. §§3(b), $\bar{O}(\mathbf{K})$ can then be recovered by sweeping the frequency between $\omega_{\min}$ and $\omega_{\max}$ so that $O(\mathbf{r})$ can then be reconstructed via an inverse K transform.

In the TD formulations with short-pulse interrogation, this DT relation is given in (§§15) and Fig. §§4. It states that the transient spectrum of the scattered field in a given spectral direction is directly related to the Radon transform of $O(\mathbf{r})$ along a direction that bisects the angle between the interrogation and the scattering directions. Thus, as illustrated there, measuring the transient scattering recovers the Radon transform of O so that $O(\mathbf{r})$ can be reconstructed via an inverse transform.

B. Filtered Backpropagation Imaging: FD Formulation

The spectral reconstruction discussed earlier may be implemented by backpropagating the data to the object domain. Backpropagation can be performed in several alternative ways, e.g., using the Kirchhoff or plane-wave integrations. The final reconstruction formulas can be expressed explicitly in terms of the backpropagated fields, regardless of the method by which they were calculated. This result will be used in Section III where the backpropagated fields are calculated via the BF formulation.

The plane-wave representation of the backpropagated fields $\hat{u}_j^b(\mathbf{r}, \omega)$, $j = 1, 2$, corresponding to the scattering data $\hat{u}_j^s(\mathbf{x}, \omega)$ measured on the z_j planes are obtained by extending (§§5) to the backpropagation domains $z > z_1$ and $z < z_2$, namely

$$\hat{u}_j^b(\mathbf{r}, \omega) = \left(\frac{k}{2\pi}\right)^2 \int_{\mathcal{P}} d^2\xi\, \hat{\tilde{u}}_j^s(\boldsymbol{\xi}, \omega) e^{ik\mathring{\boldsymbol{\kappa}}_j \cdot \mathbf{r}} \tag{1}$$

where $\mathcal{P}$ implies that the integration covers only the propagating spectrum $|\boldsymbol{\xi}| < 1$, $\hat{\tilde{u}}_j^s(\boldsymbol{\xi}, \omega)$ is the plane-wave spectrum of $\hat{u}_j^s(\mathbf{x}, \omega)$ normalized to the $z = 0$ plane, as defined in (§§4), $\mathring{\boldsymbol{\kappa}}_j = (\boldsymbol{\xi}, \mp\zeta)$ are the plane-wave directions, and $\zeta = \sqrt{1 - \boldsymbol{\xi} \cdot \boldsymbol{\xi}}$ [see (§§5)]. Here and henceforth, upper and lower signs correspond to $j = 1, 2$, respectively, i.e., to field constituents associated with the data measured on the z_j plane.

The "filtered backpropagated" or the "imaging" fields are now defined as [3]

$$\hat{I}_j(\mathbf{r}, \omega) = v_0^{-1} k^{-2} \mathring{\boldsymbol{\kappa}}^i \cdot \nabla \left[e^{-ik\mathring{\boldsymbol{\kappa}}^i \cdot \mathbf{r}} \hat{u}_j^b(\mathbf{r}, \omega) \right]. \tag{2}$$

The reconstructed media $\breve{O}_j(\mathbf{r})$ corresponding to the data $\hat{u}_j^s$ are obtained now by summing over all the frequencies, namely (see details in Appendix A)

$$\breve{O}_j(\mathbf{r}) = 2\mathrm{Re}\, \frac{1}{\pi} \int_0^\infty d\omega \hat{I}_j(\mathbf{r}, \omega). \tag{3}$$

As discussed in Sections §§III-A(4) and §§III-B, $\breve{O}_1$ and $\breve{O}_2$ correspond, respectively, to the longitudinal and transversal variations of O. If one has access to the data on both planes, then the "full reconstruction" is given by

$$\breve{O}(\mathbf{r}) = \breve{O}_1(\mathbf{r}) + \breve{O}_2(\mathbf{r}). \tag{4}$$

The UWB filtered backprojection reconstruction in (2)–(4) has been derived in [3] via a K-space formulation. For completeness, a FD derivation is presented in Appendix A.

C. Filtered Backpropagation Imaging: TD Formulation

The backpropagated fields corresponding to the time-dependent data $u_j^s(\mathbf{x}, t)$ on the z_j planes are obtained by extending (§27) to the backpropagation domains $z > z_1$ and $z < z_2$, giving

$$u_j^b(\mathbf{r}, t) = \frac{-1}{(2\pi v_0)^2} \int_{\mathcal{P}} d^2\xi\, \partial_t^2 \tilde{u}_j^s\left(\boldsymbol{\xi}, t - v_0^{-1} \mathring{\boldsymbol{\kappa}}_j \cdot \mathbf{r}\right) \tag{5}$$

where the TD plane-wave spectra $\tilde{u}_j(\boldsymbol{\xi},\tau)$ are calculated from the data $u_j^s(\mathbf{x},t)$ via (§§12), and, as in (1), the index $\mathcal{P}$ defines the integration over the propagating spectrum.

Following (2), the "filtered backpropagated" or the "imaging" fields corresponding to measurements on the z_j plane are calculated via

$$I_j(\mathbf{r},t) = -v_0 F^{\dagger}(t) \otimes \mathring{\boldsymbol{\kappa}}^i \cdot \nabla \partial_t^{-2} u_j^b\Big(\mathbf{r}, t + v_0^{-1}\mathring{\boldsymbol{\kappa}}^i \cdot \mathbf{r}\Big) \tag{6}$$

where ∂_t^{-n} defines the nth temporal integration. Here, $F^{\dagger}(t)$ is the deconvolution kernel of the interrogation pulse $F(t)$ in u^i of (§§11), defined as the inverse Fourier transform of $1/\hat{F}(\omega)$ over the data band Ω. Outside Ω, the spectrum may be continued quite arbitrarily and is typically chosen to converge smoothly to zero for $\omega \to \infty$. For a short excitation pulse, we may replace in (6) $F^{\dagger}(t) \simeq \delta(t)$ leading to

$$I_j(\mathbf{r},t) = -v_0 \mathring{\boldsymbol{\kappa}}^i \cdot \nabla \partial_t^{-2} u_j^b\Big(\mathbf{r}, t + v_0^{-1}\mathring{\boldsymbol{\kappa}}^i \cdot \mathbf{r}\Big). \tag{7}$$

The partial images reconstructed from the data on the z_j planes are obtained now via the imaging formula

$$\breve{O}_j(\mathbf{r}) = 2 I_j(\mathbf{r},t)\big|_{t=0}. \tag{8}$$

This expression is the TD counterpart of (3). As noted after (4), the TD formulation in (5)–(8) has been derived in [3] via the Radon space approach.

III. Beam-Domain DT: Multifrequency Formulation

The reconstruction formulas (2)–(3) and (7)–(8) are expressed explicitly in terms of the backpropagated fields, regardless of the calculation method of these fields. Here and in Section IV, we calculate the backpropagated fields via the FD and the TD beam formulations, respectively.

A. Backpropagation

Referring to the theory in Section §III, we start with the sets $\{\hat{\Psi}_{\boldsymbol{\mu}}^{\pm}(\mathbf{r},\omega)\}_{\boldsymbol{\mu}_P}$ of forward/backward beam propagators, where the index $\boldsymbol{\mu}_P$ defines the subset of "propagating beams." As stated in Theorem §1 of Section §III-C, each set constitutes a frame everywhere in the propagation domain, over the Hilbert space $\mathbb{H}_P$ of functions with no evanescent spectrum, with $\{\hat{\Phi}_{\boldsymbol{\mu}}^{\pm}(\mathbf{r},\omega)\}_{\boldsymbol{\mu}_P}$ being the dual-frame set. Explicit expressions for these beam propagators were given in [2], along with guidelines for constructing these sets and of choosing the various expansion parameters.

Given the scattering data $\hat{u}_j^s(\mathbf{x},\omega)$ on the z_j plane, $j = 1, 2$, the BF representation of the backpropagated fields is obtained by extending (§§16) and (§§17) to the backpropagation domains $z > z_1$ and $z < z_2$, respectively, giving

$$\hat{u}_j^b(\mathbf{r},\omega) = \sum_{\boldsymbol{\mu}\in\boldsymbol{\mu}_{\mathcal{P}}} \hat{A}_{\boldsymbol{\mu}}^j(\omega)\hat{\Psi}_{\boldsymbol{\mu}}^{\mp}(\mathbf{r},\omega), \quad z \gtrless z_j \tag{9}$$

where the expansion coefficients, defined as "the beam-domain data," are extracted from the data via (§§17)

$$\hat{A}_{\boldsymbol{\mu}}^j(\omega) = \Big\langle \hat{u}_j^s(\mathbf{x},\omega), \hat{\Phi}_{\boldsymbol{\mu}}^{\mp}(\mathbf{r},\omega)\big|_{z_j}\Big\rangle. \tag{10}$$

As noted after (1), upper and lower signs correspond to $j = 1, 2$, respectively.

The operation in (10) has been identified in (§§17) as a WFT of $\hat{u}_j^s$ over the z_j planes. Actually, as discussed there, it is somewhat more complicated than a conventional WFT; hence, it has been referred to as a BF transform.

The summation in (9) involves only the BF elements $\boldsymbol{\mu}$ in the *propagating spectrum* $\boldsymbol{\mu}_P$ [see (§11) and (§§16)]. Henceforth we omit the notation $\boldsymbol{\mu} \in \boldsymbol{\mu}_P$ in all the phase space summations (see e.g., (11), (12) etc.), since the beam-domain data $\hat{A}_{\boldsymbol{\mu}}^j(\omega)$ residing outside this range are practically zero.

B. Filtered Backpropagation and Imaging

The beam-domain reconstruction of the filtered backpropagated fields (2) is given by (see details in Appendix B)

$$\hat{I}_j(\mathbf{r},\omega) \simeq \frac{2}{i\omega} e^{-ik\mathring{\boldsymbol{\kappa}}^i\cdot\mathbf{r}} \sum_{\boldsymbol{\mu}} \hat{A}_{\boldsymbol{\mu}}^j(\omega)\cos^2\left(\frac{\gamma_{\mathbf{n}}^{\mp}}{2}\right)\hat{\Psi}_{\boldsymbol{\mu}}^{\mp}(\mathbf{r},\omega) \tag{11}$$

where $\gamma_{\mathbf{n}}^{\mp}$ is the angle between $-\mathring{\boldsymbol{\kappa}}^i$ and the scattered beam $\mathring{\boldsymbol{\kappa}}_n^{\mp}$ [see (§§31) and Fig. §§4)].

The partial images $\breve{O}_j$ are calculated now by integrating over all ω's as in (3). We shall not dwell further on these expressions and will proceed to the TD formulation that has a much richer interpretation.

IV. Beam-Domain DT: TD Formulation

A. Backpropagation

Given the scattering data $u_j^s(\mathbf{x},t)$ on the z_j plane, $j = 1, 2$, the BF representation of the backpropagated fields is obtained by extending (§§23) and (§§24) to the backpropagation domains $z > z_1$ and $z < z_2$, respectively, giving

$$u_j^b(\mathbf{r},t) = \sum_{\boldsymbol{\mu},s} A_{\boldsymbol{\mu},s}^j \Psi_{\boldsymbol{\mu},s}^{\mp}(\mathbf{r},t) \tag{12}$$

where the expansion coefficients that are referred to as "the beam-domain data" are extracted from the data via

$$A_{\boldsymbol{\mu},s}^j = \Big\langle u_j^s(\mathbf{x},t), \Phi_{\boldsymbol{\mu},s}^{\mp}(\mathbf{r},t)\big|_{z_j}\Big\rangle_{(\mathbf{x},t)}. \tag{13}$$

The operation in (13) has been identified in (§§24) as a WRT of u_j^s in the $(\mathbf{x},t)$ domain corresponding to the z_j planes, as schematized in Fig. §§6. Actually, it is somewhat more complicated than a WRT; hence, it has been referred to as a PBF transform.

B. Filtered Backpropagation and Imaging

The expressions for the filtered backpropagated fields are derived by inserting (12) into (7) and using the fact that the beams are collimated (see (11) and Appendix B), obtaining

$$I_j(\mathbf{r},t) = -2\sum_{\boldsymbol{\mu},s} A_{\boldsymbol{\mu},s}^j \cos^2\left(\frac{\gamma_{\mathbf{n}}^{\mp}}{2}\right)\partial_t^{-1}\Psi_{\boldsymbol{\mu},s}^{\mp}\big(\mathbf{r}, t + t^i(\mathbf{r})\big) \tag{14}$$

where $t^i(\mathbf{r}) \stackrel{\text{def}}{=} v_0^{-1}\mathring{\boldsymbol{\kappa}}^i \cdot \mathbf{r}$ is the arrival time of the incident pulse at $\mathbf{r}$, as defined in (§§27). Note that this result can also

be derived by transforming (11) into the TD and using the representation in (§34).

The partial images are then calculated via (8) by setting the imaging condition $t = 0$, giving

$$\breve{O}_j(\mathbf{r}) = \sum_{\boldsymbol{\mu},s} A^j_{\boldsymbol{\mu},s}\breve{\Lambda}^j_{\boldsymbol{\mu},s}(\mathbf{r}) \tag{15}$$

where the "imaging kernels" are

$$\breve{\Lambda}^j_{\boldsymbol{\mu},s}(\mathbf{r}) = -4\cos^2\left(\frac{\gamma^{\mp}_{\mathbf{n}}}{2}\right)\partial_t^{-1}\Psi^{\mp}_{\boldsymbol{\mu},s}\left(\mathbf{r}, t^i(\mathbf{r})\right). \tag{16}$$

Finally, if the scattering data are available on both the $j = 1$ and 2 planes then $\breve{O} = \breve{O}_1 + \breve{O}_2$ as in (4).

Equation (15) expresses the reconstructed image at a given $\mathbf{r}$ by aggregating the contributions of the beam-domain data $A^j_{\boldsymbol{\mu},s}$ weighted by the "imaging kernels" $\breve{\Lambda}^j_{\boldsymbol{\mu},s}(\mathbf{r})$. One readily observes from (16) that $\breve{\Lambda}^j_{\boldsymbol{\mu},s}$ have essentially the same structure as $\Lambda^j_{\boldsymbol{\mu},s}(\mathbf{r})$ in (§§27). Referring to the illustration in Fig. §§6, they are centered along the $\boldsymbol{\mu}$-axes, with the location along the axes determined by t_s via (§§28) and (§§29) (see Fig. 1 as well). In view of the $t^i(\mathbf{r})$ term in (16), the windows are rotated relative to the $\boldsymbol{\mu}$-axes such that they are orthogonal to the direction $\mathring{\mathbf{s}}^{\mp}_{\mathbf{n}}$ that bisects the angle $\gamma^{\mp}_{\mathbf{n}}$ between the direction of incidence $-\mathring{\boldsymbol{\kappa}}^i$ and the $\boldsymbol{\mu}$ axis [see analysis in (§§30)–(§§32)]. In view of the window localization, it is sufficient to account only for the PBs that pass near $\mathbf{r}$. Based on previous studies on the PB summation method, we consider only the windows whose centers are within a three-beamwidth and three-pulsewidth zone about $\mathbf{r}$.

Finally, following the discussion in Section §§V-C, one may regard the local reconstruction formula in (15) as an inverse of the LRT of the object, which is illustrated in Fig. §§6.

C. ID Phase-Space Processing

As discussed in Section §§V-D, we perform the phase-space processing using the ID propagators. Explicit expressions for these propagators in 3-D and 2-D configurations were given in Appendixes §A–§C, along with criteria for choosing the various parameters in these expressions. Specific considerations for choosing these parameters in the context of phase-space processing have been discussed in Section §§V-D and also in the numerical examples of Section §§VI-B. The same values should be used here for the reconstruction problem. We, therefore, present here only the expression for the imaging kernels $\breve{\Lambda}^j_{\boldsymbol{\mu},s}(\mathbf{r})$.

For 3-D configurations, we substitute $\Psi^{\mp}_{\boldsymbol{\mu},s}$ from (§B5) in (16), obtaining

$$\begin{aligned}\breve{\Lambda}^j_{\boldsymbol{\mu},s}(\mathbf{r}) = -4\cos^2\left(\frac{\gamma^{\mp}_{\mathbf{n}}}{2}\right)\mathrm{Re}\left\{\sqrt{\frac{-i\,F_{\boldsymbol{\mu}1}}{z_{b_{\boldsymbol{\mu}}}-i\,F_{\boldsymbol{\mu}1}}\frac{-i\,F_{\boldsymbol{\mu}2}}{z_{b_{\boldsymbol{\mu}}}-i\,F_{\boldsymbol{\mu}2}}}\right.\\ \times e^{i\alpha}\overset{+}{\Upsilon}{}^{(\gamma-1)}\left(\frac{\mathring{\boldsymbol{\kappa}}^i\cdot\mathbf{r}}{v_0}-\frac{z_{b_{\boldsymbol{\mu}}}}{v_0}-t_s\right.\\ \left.\left.-\frac{x^2_{b_{\boldsymbol{\mu}1}}/2v_0}{z_{b_{\boldsymbol{\mu}}}-i\,F_{\boldsymbol{\mu}1}}-\frac{x^2_{b_{\boldsymbol{\mu}2}}/2v_0}{z_{b_{\boldsymbol{\mu}}}-i\,F_{\boldsymbol{\mu}2}}\right)\right\}\end{aligned} \tag{17}$$

where the beam coordinates $(z_{b_{\boldsymbol{\mu}}}, \mathbf{x}_{b_{\boldsymbol{\mu}}})$ and the collimation lengths $F_{\boldsymbol{\mu}1,2}$ are defined in (§A4 and §A5).

For 2-D configurations, we use $\Psi^{\mp}_{\boldsymbol{\mu},s}$ from (§C4), obtaining

$$\begin{aligned}\breve{\Lambda}^j_{\boldsymbol{\mu},s}(\boldsymbol{\rho}) = -4\cos^2\left(\frac{\gamma_{\mathbf{n}}}{2}\right)\mathrm{Re}\left\{\sqrt{\frac{-i\,F_{\boldsymbol{\mu}}}{z_{b_{\boldsymbol{\mu}}}-i\,F_{\boldsymbol{\mu}}}}\right.\\ \left.\times e^{i\alpha}\overset{+}{\Upsilon}{}^{(\gamma-1)}\left(\frac{\mathring{\boldsymbol{\kappa}}^i\cdot\boldsymbol{\rho}}{v_0}-\frac{z_{b_{\boldsymbol{\mu}}}}{v_0}-t_s-\frac{x^2_{b_{\boldsymbol{\mu}}}/2v_0}{z_{b_{\boldsymbol{\mu}}}-i\,F_{\boldsymbol{\mu}}}\right)\right\}\end{aligned} \tag{18}$$

where $\boldsymbol{\rho} = (x, z)$, as defined in (§20).

The various parameters used in (17) and (18) are explained after (§§34) in the context of the phase-space processing windows, along with the considerations for choosing these parameters. As noted earlier, the same values should be used for the imaging kernels considered here. Specifically, as discussed after (§§34), the preferred values for (α, γ) are $\alpha = \pi/2$ or 0 for even or odd γ, respectively. Following similar analysis, one may show that these values render the kernels in (17) and (18) localized and symmetric about their axes, as desired.

V. Numerical Example A: Sparsely Inhomogeneous Medium

This example is a continuation of the example in Section §§VI of Part I of this article, where we calculated the beam-domain data via phase-space processing. The inhomogeneity here is taken to be rather sparse in order to simplify the interpretation of the results. In Section VI, we shall consider a more complicated medium as well as the use of several illumination directions to achieve a better resolution and to filter out the noise.

A. Problem Setup

We refer to the 2-D configuration described in Section §§VI-A and Fig. §§7, where the $[-20, 20] \times [-20, 20]$ DoI is marked as a black rectangle. Space–time units are taken such that the background wave speed $v_0 = 1$. As defined in Part I of this article, the illumination is the pulsed plane wave in (§§11) that propagates along the z-axis, whose frequency band is $\boldsymbol{\Omega} = [\omega_{\min}, \omega_{\max}] = [0.1, 1]$ so that its pulselength is $T_0 \approx 2\pi$. Note that the problem is large on the pulselength scale and that the contrast is quite large and is of the order of 40%.

We consider here only the reflection data at $z_{\mathrm{l}} = -150$ within the measurement aperture $|x| < 250$. These data have been calculated via the method of moments (MoM).

Finally, we remark, again, that these data are insufficient for reconstructing general medium, but it is appropriate for the media in this section and in Section VI that are characterized by strong longitudinal variation but a weak transversal variation.

Our main goal in this article is the formulation of the beam-domain processing and filtered backpropagation algorithms within the DoI. Accordingly, we considered only illuminations from the z_{l} plane and measurement of the reflected

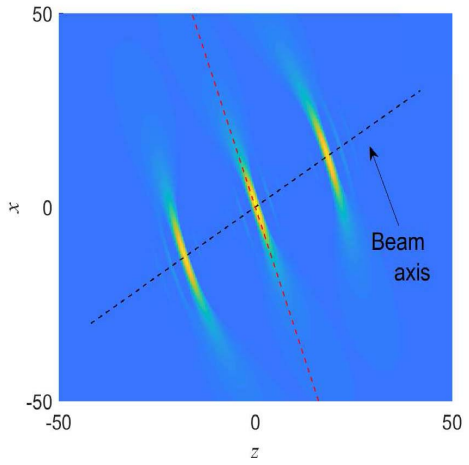

Fig. 1. Imaging kernels $\breve{\Lambda}^{j}_{\boldsymbol{\mu},s}(\mathbf{r})$ for a fixed $\boldsymbol{\mu}$ and several values of s.

field within a limited aperture in that plane. As discussed in Section §§III-A4 [see also Fig. §§3(b)], these data are insufficient for the reconstruction of a general medium, and it is more appropriate for reconstruction of media with dominant longitudinal variation and weak transversal variation. Thus, the numerical examples chosen in Sections V and VI are aimed at exploring the features of reconstruction subject to these constraints. Note that this class of problems is of interest per se in many applications.

B. Phase-Space Processing: Beam-Domain Data

The phase-space processing of the data has been discussed in Section §§VI-B, along with a detailed discussion regarding the choice of the various parameters used for the processing windows [i.e., $(\bar{x},\bar{\xi})$, $\nu_{\max}$, b, and (α,γ)]. The resulting beam-domain scattering data have been discussed and interpreted in Section §§VI-C and Figs. §§9 and §§10.

C. Imaging Kernels

The 2-D imaging kernels $\breve{\Lambda}^{j=1}_{\boldsymbol{\mu},s}(\boldsymbol{\rho})$ of (16) are given in (18). As noted earlier, we use the same parameters as those used in the phase-space processing of the data in Section §§VI-B.

Fig. 1 depicts a few examples of $\breve{\Lambda}^{j=1}_{\boldsymbol{\mu},s}$ for a fixed $\boldsymbol{\mu}$ and several values of s. As discussed after (16), $\breve{\Lambda}^{j}_{\boldsymbol{\mu},s}$ are localized along the beam axis and are tilted in the $\mathring{\boldsymbol{s}}^{-}_{\mathbf{n}}$ direction (blue arrow) that bisects the angle between the $\boldsymbol{\mu}$ beam-axis and the interrogation direction $-\mathring{\boldsymbol{\kappa}}^{i}$.

D. Local Reconstruction: Single Illumination

The reconstructed medium inside the DoI is calculated via (15), where only those PB backpropagators that pass within a three beamwidths distance from the DoI were included in the $(\boldsymbol{\mu},s)$ summation. As noted in Section V-A, we calculate only $\breve{O}_1$ using the reflection data at $z_1=-150$.

The reconstructed medium $\breve{O}_1(\boldsymbol{\rho})$ within the DoI is depicted in Fig. 2(b), along with the reconstruction error in Fig. 2(c). Inside the DoI, $\breve{O}_1(\boldsymbol{\rho})$ agrees quite well with the scattering

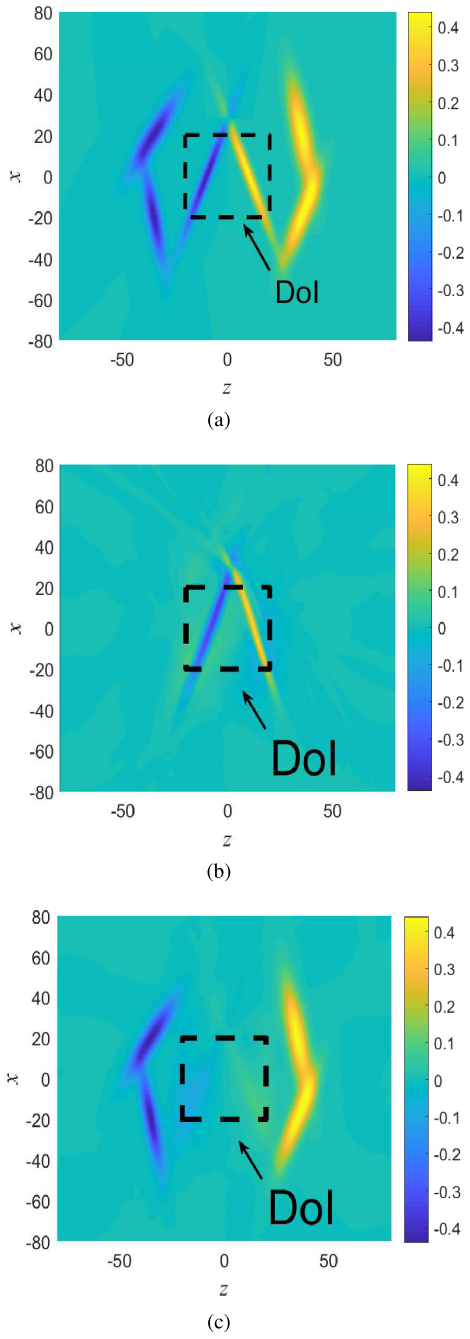

Fig. 2. Local reconstruction of example A. (a) Original medium $O(\boldsymbol{\rho})$. (b) Reconstructed medium $\breve{O}_1(\boldsymbol{\rho})$ (i.e., using only data at z_1). (c) Reconstruction error $O(\boldsymbol{\rho})-\breve{O}_1(\boldsymbol{\rho})$. Note the large "error" outside the DoI, as expected.

medium in Fig. 2(a), while outside the DoI, $\breve{O}_1(\boldsymbol{\rho})$ gradually vanishes, as expected.

A more detailed analysis is depicted in Fig. 3, where we plot cross-sectional cuts of $\breve{O}_1(\boldsymbol{\rho})$ along the lines $x=0$ and $x=5\approx\bar{x}/2$, respectively. The results are shown only within the DoI $z\in[-20,20]$. As can be discerned, the reconstruction, referred to in the figures as "iter-1" (purple dashed lines), recovers pretty good both the shapes and composition of the layers, but it suffers from an axial displacement error. This error stems from the fact that the imaging kernels are based on

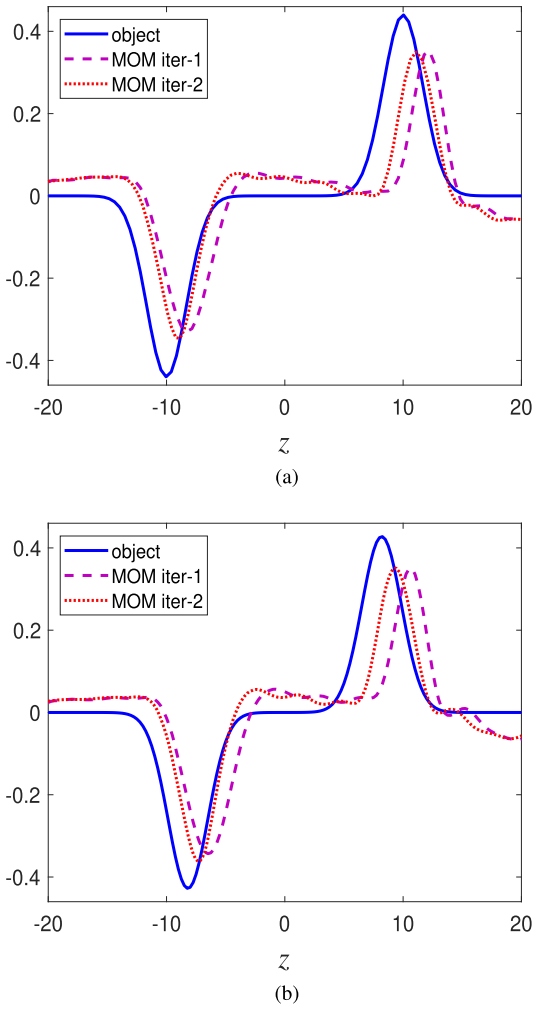

Fig. 3. Cross-sectional cut of the reconstruction along the lines. (a) $x = 0$. (b) $x = 5$. Blue solid lines: the physical medium. Purple dashed and red dashed-dotted lines: reconstruction based on the MoM data after one and two iterations, respectively.

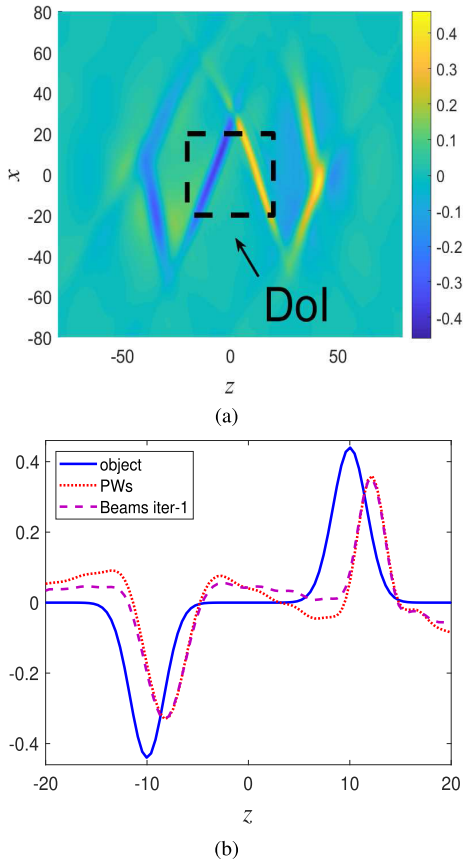

Fig. 4. Comparison of the beam-based inverse scattering algorithm and the conventional plane-wave-based DT. (a) Reconstructed medium using plane-wave processing. (b) Cross-sectional cuts of the medium along the line $x = 0$. Blue solid lines: physical medium. Purple dashed and red solid lines: reconstruction using the first iteration in the beam-based algorithm and using the plane-wave algorithm, respectively. In both cases, we used exact MoM data.

free-space propagation, whereas, in reality, the scattered waves propagate in an inhomogeneous medium, and it is significantly large since the contrast in our example is much larger than what is typically used in the Born approximation.

This displacement error is partially mitigated by employing an iterative scheme where the travel time along the axis of each backpropagated beam is corrected using the medium reconstructed in the previous iteration. Specifically, we use the velocity that is reconstructed from $\breve{O}_1(\boldsymbol{\rho})$ to fix the travel time along the axes of the backpropagated beams $\Psi^{-}_{\boldsymbol{\mu},s}(\boldsymbol{\rho}, t)$ and of the imaging times $t^i(\boldsymbol{\rho})$, which together defines the imaging kernels $\breve{\Lambda}^{j=1}_{\boldsymbol{\mu},s}(\boldsymbol{\rho})$ of (16) used in the reconstruction formula (15). One readily observes that the displacement error is reduced in the second iteration, denoted in Fig. 3 as "iter-2" (red dashed-dotted lines). Note, though, that the improvement is limited since we use the corrected wave speed only inside the DoI.

To clarify the source of errors in the imaging algorithm, we compare the beam-based approach to the conventional plane-wave approach. The latter can be implemented via the spectral reconstruction approach discussed in Section II-A, but, here, we used the equivalent filtered backpropagation algorithm of [3] discussed in Section II-B. We use the same data set discussed in Section V-A. The imaging results are depicted in Fig. 4(a). The beam-based and the plane-wave processing results are compared in Fig. 4(b), where, for the former, we consider only the first iteration in Fig. 3(a). Note the good agreement inside the DoI, while outside the DoI, the beam-based image is irrelevant since it actually excludes the beam-backpropagators there. Note that a clear advantage of the beam-based approach is that it is amenable for an iterative correction of the travel time along the beam axis, as done in Fig. 3.

Further insight into the sources of error is obtained by comparing in Fig. 5 the reconstructions using the exact data and the Born approximated data (which is calculated analytically, see Appendix C). In principle, using this synthetic data, we should have obtained an exact reconstruction if the data were known for all x at both the z_1 and z_2 planes. Thus, the reconstruction error is mainly due to the limited view angles (only reflection data at an aperture of approximately $\pm 45°$), while the small dc error is attributed also to the missing low frequencies as also follows from the

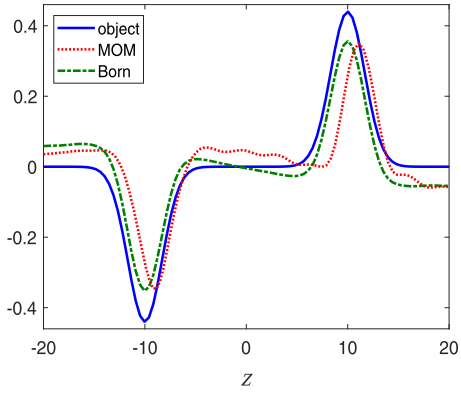

Fig. 5. Cross-sectional cut of the reconstruction along the line $x = 0$. Blue solid line: physical medium. Red dashed-dotted lines: reconstruction based on the exact MoM data after two iterations. Green dotted lines: reconstruction using plane-wave processing and Born-approximated data.

TABLE I
PARAMETERS OF THE MEDIUM IN FIG. 6(a)

l	n_l	x_l	z_l	θ_l	σ_{1_l}	σ_{2_l}
1	1.2	0	2.5	$\pi/9$	$10\sqrt{5}$	$\sqrt{5/2}$
2	0.75	0	-2.5	$-\pi/9$	$10\sqrt{5}$	$\sqrt{5/2}$
3	1.2	5	10	$\pi/18$	$\sqrt{350}$	$\sqrt{10}$
4	1.2	-5	-10	$\pi/18$	$5\sqrt{10}$	$\sqrt{5}$
5	0.75	-5	15	$-\pi/9$	$5\sqrt{10}$	$\sqrt{15/2}$
6	0.75	5	-15	$-\pi/6$	$10\sqrt{2}$	$\sqrt{15/2}$.

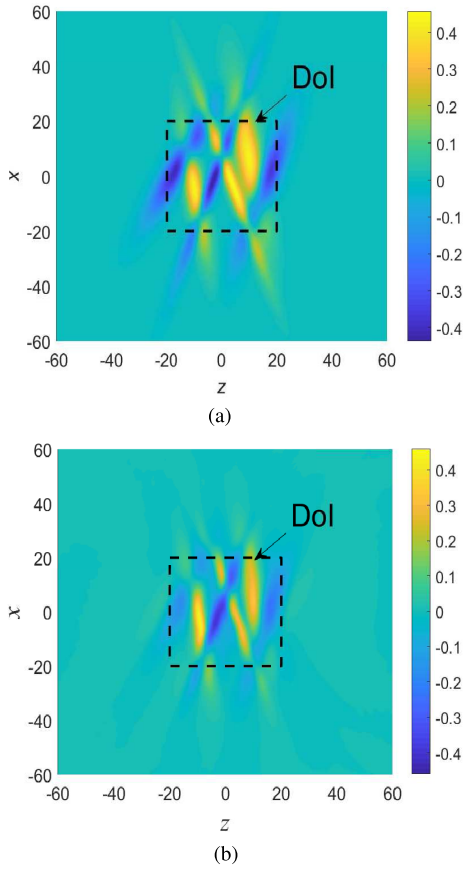

Fig. 6. Reconstruction of the medium in Table I using single-axial illumination. (a) Original medium $O(\boldsymbol{\rho})$. (b) Reconstructed medium $\mathring{O}_1(\boldsymbol{\rho})$ in the DoI.

basic DT considerations in Section §§III-A(4) and Fig. §§3(b) (see the missing K-space data in Fig. 8). The reader is also referred to as the TD interpretation of the data in Fig. §§4.

Finally, we note that we do not provide here a quantitative measure of the error in terms of its norm. As discussed earlier, the main error in our examples is a displacement error that is due to the relatively large contrast used (see also the more complicated examples in Figs. 7–9). Quantifying such displacement error using $\mathbb{L}_1$ or $\mathbb{L}_2$ norms is somewhat irrelevant, whereas the cross-sectional cuts of the error in Figs. 3 and 4(b) provide a clearer qualitative understanding of the error.

VI. Numerical Example B: Denser Inhomogeneous Medium and Noisy Data

A. Problem Setup

In the example given in Section V, we considered a sparse inhomogeneity; in that case, the interpretation of the results is simple. Next, we consider a denser inhomogeneity, as shown in Fig. 6(a). Specifically, the medium is given by (§§35) where the parameters are now described in Table I (compare Table §§I for the parameters of the example of Section V). As defined in Section V, the units are taken such that the background wave speed $v_0 = 1$, with the $[-20, 20]\times[-20, 20]$ DoI marked as a black rectangle in the figure.

In order to enhance the resolution and to filter out the noise, we shall use several independent illumination directions. Such data can be synthesized by using an array of point transducers located at the points x_p on the z_1 plane and measure the scattered fields $u^s_{q,p}(t)$ at the q receiver due to an excitation of the p source, where (p, q) are indexes. Specifically, we use $z_1 = -150$ and $x_p = pd$ with the interelement spacing $d = 1.15\pi$ and $p = -(P-1)/2, \ldots, (P-1)/2$, $P = 139$, such that the measurement aperture is $|x| < D/2$ with $D = 500$. The sources are excited individually by a pulse $F'(t)$ whose frequency band is $\Omega = [\omega_{\min}, \omega_{\max}] = [0.1, 1]$, as discussed in Section V-A. Note that since the array is "far" from the tested medium, the interelement spacing can be parser than the Nyquist condition $d = \lambda$. Without loss of generality, we use the same array to measure the scattering data, which is calculated numerically via the MoM.

These data are now stacked as

$$u^s_{q,i}(t) = \sum_p 2d v_0^{-1} \zeta^i u^s_{q,p}\left(t - v_0^{-1} \mathring{\boldsymbol{\kappa}}^i \cdot \boldsymbol{\rho}_p\right) \tag{19}$$

where $\boldsymbol{\rho}_p = (x_p, z_1)$ are the source coordinates, and $\kappa^i = (\xi^i, \zeta^i) = (\sin\theta^i, \cos\theta^i)$ is the desired wave-direction with i being an index. It can be shown that $u^s_{q,i}(t)$ of (19) represents, synthetically, the response at sensor q due to an incident plane wave of the form

$$u^i(\boldsymbol{\rho}, t) = F\left(t - v_0^{-1} \mathring{\boldsymbol{\kappa}}^i \cdot \boldsymbol{\rho}\right) \tag{20}$$

where, as in (§§11), the plane wave is normalized with respect to the origin. In Section VI-C, we shall apply (19) for several wave-directions $\mathring{\boldsymbol{\kappa}}^i$. Note that due to the finite

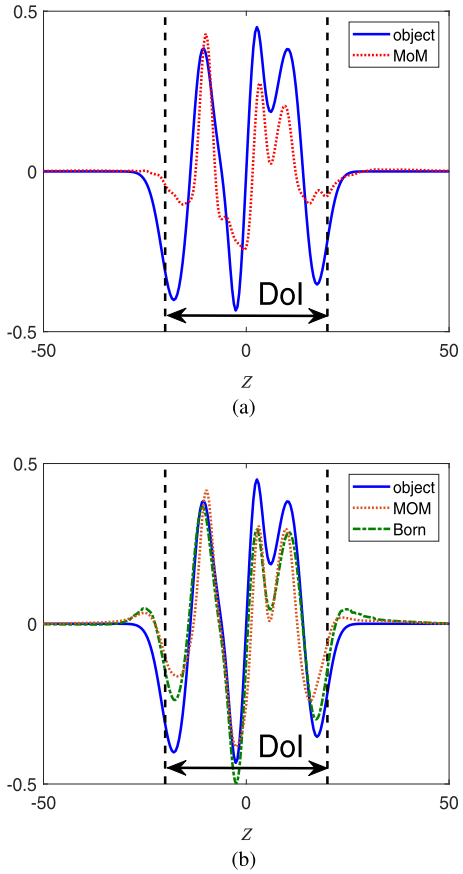

Fig. 7. Cross-sectional cuts of the reconstruction along the line $x = 0$. (a) Reconstruction from a single illumination at $\theta^i = 30°$. Red dotted line: MoM data. Green solid line: Born data. In both cases, we used the beam-based algorithm with two iterations. (b) Reconstruction using several illuminations $\theta^i = 0°, \pm 15°$, and $\pm 30°$. In the legend of both (a) and (b), write MoM data, iter = 2 for the red line and Born data for the green line.

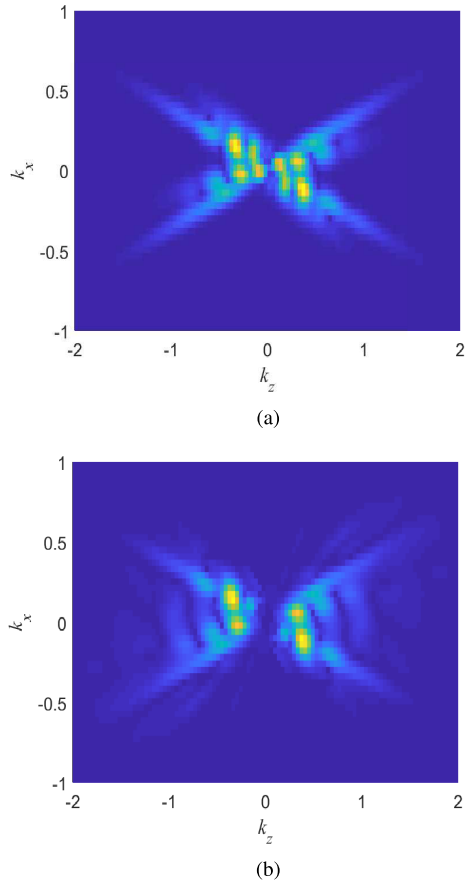

Fig. 8. K-space distribution of the object. (a) Original medium $\bar{O}$. (b) Reconstructed medium $\breve{O}_1$.

size of the array, the plane wave angles will be limited to $\theta^i \approx \pm 40°$. The synthetic plane-wave data in (19) are then processed and backpropagated to form the image using the phase-space kernels discussed in Sections V-B and V-C and the second-order iterative scheme discussed in connection with Fig. 3.

B. Single Illumination

We consider first a single illumination at an angle $\theta^i = 30°$ with respect to the z-axis. The reconstruction results are shown in Fig. 6(b), with a cross-sectional cut of the reconstructed medium in Fig. 7(a). One observes a good reconstruction for the layers with positive O but a large error for those with negative O. This difference is clearly explained physically in terms of the missing data. We note that the layers with positive and negative O [marked yellow and blue in Fig. 6(a)] have a positive and negative slant of $+20°$ and $-30°$, with respect to the x-axis, respectively (see column 5 in Table I). Taking into account the generalized Snell law discussed in Figs. §§4 and §§6 and the direction of the incident plane wave, it follows that the PB is scattered by the positively slanted layers (yellow) that propagate essentially at angles around $-10°$ with respect to the $-z$-axis, whereas those that are scattered by the negatively slanted layers (blue) propagate at an angle around 80° and are, therefore, outside our measurement aperture, so there is only weak data on these layers.

In order to explain this difference further, we compare in Fig. 8(a) the K-space distributions $\bar{O}(\mathbf{K})$ and $\bar{O}_1(\mathbf{K})$ where the former is the K-space distributions (§§8) of $O(\boldsymbol{\rho})$, while the latter is the distribution corresponding only to the data on the z_1 plane, as defined in (§§7) [see Figs. §§2(b) and §§3(b)]. One readily discerns that the main difference is in the range $|\mathbf{K}| \approx 0$, which cannot be recovered from the "reflection-type" measurements on the z_1 plane, as discussed in Fig. §§3(b) and (§§9). Recovering these data requires "transmission-type" measurements on the z_2 plane or multiple illumination angles, as will be done next.

C. Using Several Illuminations: Noise Cancelation

The single illumination reconstruction error noted in Fig. 7(a) may be mitigated by superimposing the reconstructed media due to several illumination directions. An example is shown in Fig. 7(b) where we used $\theta^i = 0°$, $\pm 15°$, and $\pm 30°$. Here, the upward-/downward-propagating waves contribute to the reconstruction of the layers with positive/negative slopes, respectively. As earlier, we also show the reconstruction using the Born approximated data, which can be regarded as the theoretical limit of the reconstruction.

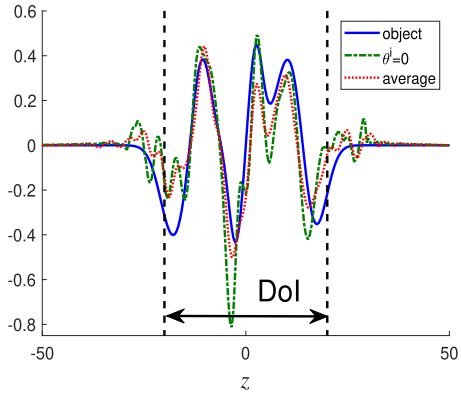

Fig. 9. Reconstruction from noisy data, plotted only along the $x = 0$ line. Blue solid line: physical medium. Green dashed lines: reconstruction from a single illumination at $\theta^i = 0°$. Red dashed lines: reconstruction using five independent illuminations at $\theta^i = 0°, \pm 15°, \pm 30°$.

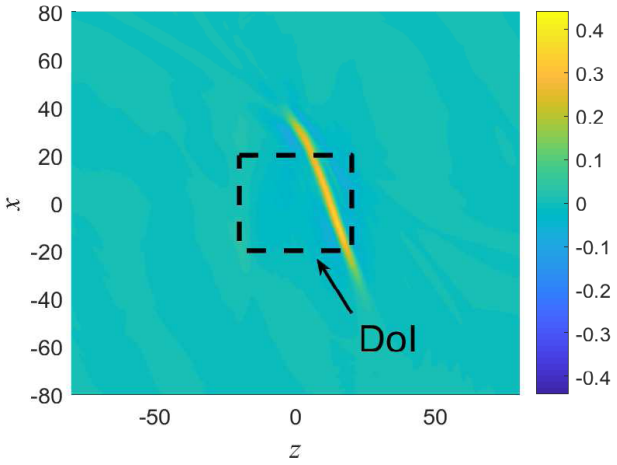

Fig. 10. Reconstruction using only the beams with negative n.

As discussed earlier, this error could have been eliminated if we had also data from the z_2 plane.

The use of several independent illuminations is also used to mitigate the effect of noise in the data. The spectrum of the data $\hat{u}^s_{q,p}$ in (19) is taken to be

$$\hat{u}^s_{pq} = \hat{u}^{s0}_{pq}\,(1 + n_c)\,, \quad n_c = n_r + i n_i, \quad n_r, n_i \sim \mathcal{N}\left(0, \sigma_n^2\right) \tag{21}$$

where $\hat{u}^{s0}_{q,p}$ is the noiseless data calculated via the MoM. Here, n_r and n_i are both normally distributed with zero mean and σ_n^2 standard deviation, such that $|n_c|$ is a Rayleigh distribution with mean $\sigma_n\sqrt{\pi/2}$ and standard deviation $\sigma_n\sqrt{2-\pi/2}$. Henceforth, we use $\sigma_n = 10$, corresponding to signal to noise level of -22 dB.

Fig. 9 compares the reconstructed medium using a single illumination at $\theta^i = 0°$ to the results obtained by averaging the media reconstructed using five independent illuminations at $\theta^i = 0°$, $\pm 15°$, and $\pm 30°$. One observes that the noise error in the multiple illumination processing is reduced compared with the single illumination case such that the result tends to the noiseless case in Fig. 7(b). This stems from the fact that the overall SNR of the image is governed by $20 \log \sigma_n^{-1} \sqrt{2/\pi}\sqrt{N_t}$, where N_t is the overall number of independent illuminations and points where the data are sampled [6, Eq. 30].

D. Phase Space Filtering

The beam-domain backpropagation and imaging may be used to focus on specific local wave mechanisms in the medium. As an example, we refer, again, to the configuration in Fig. §§7, which is illuminated by a pulsed plane wave along the z-axis as in Section V-A. The beam-domain scattering data $A^{j=1}_{\boldsymbol{\mu},s}$ have been presented and discussed in Fig. §§9. Here, we would like to identify only on the downward sloping layers; hence, we keep in (15) only the subset of negative n coefficients in Fig. §§9. The resulting reconstruction in Fig. 10 clearly demonstrates the spatial filtering of the desired features.

VII. Conclusion and Overall Summary

In this two-part article, we considered an UWB local DT where beam-waves are used for local (phased-space) processing and expansion of the scattering data and then for local backpropagation and imaging. The key feature of the beam approach is that it enables backpropagation over an inhomogeneous medium while focusing on any desired subdomain of interest (DoI). We derived two algorithms: one is expressed in the multi-FD, and the other is applied directly in the short-pulse TD.

The key features that facilitate the beam-expansion approach are as follows:

1) the use of an ID beam set where both the beam skeleton and the propagation parameters are frequency-independent so that they can be calculated once and then used for all frequencies or expressed directly in the TD;
2) the fact that the phase-space beam sets constitute frames everywhere in the propagation domain so that these BFs can be used to expand both the medium and the scattered fields.

The beam-based imaging algorithm consists of two phases: a preprocessing phase where the scattering data is transformed into the beam domain, and an imaging phase where these data are backpropagated locally to reconstruct the medium. These two phases are studied in Parts I and II.

Part I of this article deals with the representation of the data in the beam domain. The expansion coefficients $A^j_{\boldsymbol{\mu},s}$, referred to as the beam-domain data, are calculated from the scattered fields using windowed phase-space transforms, the generalized WFT in (§§16) and (§§17), and the generalized WRT in (§§23) and (§§24) for the multifrequency and the TD formulations, respectively. In these expressions, the sets $\{\Psi^{\pm}_{\boldsymbol{\mu},s}(\mathbf{r}, t)\}$ and $\{\Phi^{\pm}_{\boldsymbol{\mu},s}(\mathbf{r}, t)\}$ are shown to be dual-frame sets and used, respectively, as the forward/backward beam propagators and corresponding processing windows. Specifically, we use the ID beam sets that are given explicitly in Appendixes §A–§C.

A key result of Part I of this article has been the derivation of the "local TD DT identity," according to which the

beam-domain data noted earlier is directly related to local projections of the medium function onto windows that are formed by the PB propagators as they traverse through the medium (see (§§26) and Fig. §§6). This operation, termed there LRT of the medium (see footnote 3 for a comment on the terminology), extracts the local stratification of the medium. As such, it has a cogent physical interpretation as a local generalized Snell's law, according to which the PBs that are scattered at any given point and direction are generated by the local stratification of the medium used there in a direction that bisects the angle between the directions of incidence and scattering.

This fundamental result has been used in this Part II for the local reconstruction of the medium via beam-domain filtered backpropagation. This operation is defined in (11) and (14) for the multifrequency and the TD formulations, respectively. The reconstructed medium at any point is then obtained by aggregating the contributions of the backpropagated beams that pass near that point [see (15) and (16)]. Specific expressions for the ID imaging kernels $\breve{\Lambda}^{j}_{\boldsymbol{\mu},s}(\mathbf{r})$ are given in (17) and (18) for 3-D and for 2-D configurations, respectively.

The local processing approach enables the user to concentrate on any desired DoI and filter out the scattering data (and noise) arriving from other regions in the scattering domain. Furthermore, utilizing the local structure of the beams, we introduced an iterative correction scheme where the reconstruction results are used to fine-tune the beam backpropagators. The implementation of this approach is actually simpler than that of the distorted Born reconstruction [8] since it requires only simple corrections along the axes of the beam backpropagators. The beam approach may, therefore, be used for complicated objects with relatively large contrast compared with conventional plane-wave-based DT.

The intricate analytic details of the algorithms and the choice of the expansion parameters have been thoroughly discussed and demonstrated in the numerical examples in Parts I and II, as well as in [2]. These examples also elucidate the physical interpretation and the content of the beam-domain data. Specifically, we considered reconstruction using only reflection data from a limited spectrum of illumination directions; in that case, it follows from the basic theory of DT (see Sections §§III-A(4) and §§III-B) that the objects that can be reconstructed are quasi stratified, such as those depicted in Figs. §§2(a) and §§6(a). It has been shown that the beam approach with the first-order correction leads to a better reconstruction of objects with large contrast compared with the conventional plane-wave approach.

Finally, we note that the imaging problem of sparse point scatterers can be addressed also by SVD-based formulations, such as MUSIC and time reversal (see a literature survey in [7]). These methods typically do not scale well with the problem size, but by performing this analysis on the beam-domain data, as in [7], one may focus *a priori* on the data corresponding to a given DoI and, thus, mitigate the size difficulty. In that context, it should be noted that our method beam-based filtered backpropagation imaging algorithms have recently been applied successfully for a realistic seismic inversion in [9].

APPENDIX A
DERIVATION OF (3)

A. Backpropagated Field

As noted in (1), the backpropagated fields $\hat{u}^b_j(x)$ have only propagating spectral constituents. Their K-space distribution, defined via (§§8), are, therefore, confined to the Ewald sphere $|\mathbf{K}| = k = \omega/v_0$, i.e., they have the form

$$\hat{\bar{u}}^b_j(\mathbf{K}) = \hat{\bar{u}}^b_j(\mathbf{K})\,\delta\left(|\mathbf{K}| - k\right), \quad \mathbf{K} = \left(K_{x_1}, K_{x_2}, K_z\right) \tag{A.1}$$

where, as in (§§8), the overbar denotes the functions in the 3-D K-domain. Next, we note that

$$\delta\left(|\mathbf{K}| - k\right) = \frac{k}{k_z}\left[\delta\left(K_z - k_z\right) + \delta\left(K_z + k_z\right)\right] \tag{A.2}$$

with

$$k_z(\mathbf{K}_x) = \sqrt{k^2 - |\mathbf{K}_x|^2}, \quad \mathbf{K}_x = \left(K_{x_1}, K_{x_2}\right) \tag{A.3}$$

where the square root is defined to be positive. We, therefore, identify

$$\hat{\bar{u}}^b_j(\mathbf{K}) = \frac{k}{k_z}\hat{\bar{u}}^b_j(\mathbf{K})\delta\left(K_z \pm k_z\right) \tag{A.4}$$

where, as noted earlier, upper and lower signs correspond to $j = 1, 2$, respectively.

The spatial representation of the backpropagated field is obtained by inverting (A.4) via (§§8), obtaining

$$\begin{aligned}\hat{u}^b_j(\mathbf{r}) &= \frac{1}{(2\pi)^3}\int d^3K e^{i\mathbf{K}\cdot\mathbf{r}}\hat{\bar{u}}^b(\mathbf{K}) \\ &= \frac{1}{(2\pi)^3}\int d^2K_x e^{i\mathbf{K}_x\cdot\mathbf{x}} \\ &\quad\times\int dK_z\frac{k}{k_z}\hat{\bar{u}}^b_j(\mathbf{K})\delta\left(K_z \pm k_z\right)e^{iK_z z} \\ &= \frac{1}{(2\pi)^3}\int d^2K_x e^{i\mathbf{K}^{\pm}\cdot\mathbf{r}}\frac{k}{k_z}\hat{\bar{u}}^b_j\left(\mathbf{K}^{\pm}\right)\end{aligned} \tag{A.5}$$

where $\mathbf{K}^{\pm}(\mathbf{K}_x) = (\mathbf{K}_x, \pm k_z(\mathbf{K}_x))$, with $|\mathbf{K}_x| < k$, denote the respective points on the right and left Ewald hemispheres, respectively [see Fig. §§2(b)]. Replacing $\mathbf{K}_x \to k\boldsymbol{\xi}$ and $k_z \to k\zeta$, assuming $k > 0$, and comparing (A.5) to (1), we find that

$$\hat{\bar{u}}^b_j(\mathbf{K}) = 2\pi\zeta\hat{\bar{u}}^s_j(\boldsymbol{\xi}) \qquad \text{for } \mathbf{K} = k\mathring{\boldsymbol{\kappa}}_j \tag{A.6}$$

with $\mathring{\boldsymbol{\kappa}}_j$ defined in (1).

B. Data-Object Relation in the Weak Scattering Approximation

Next, we use the weak scattering (Born) approximation for the data whose K-space representation is given (§§7). Inserting into (A.6), we obtain

$$\hat{\bar{u}}^b_j(\mathbf{K}) = i\pi k\bar{O}\left(\mathbf{K} - k\mathring{\boldsymbol{\kappa}}^i\right)\delta\left(|\mathbf{K}| - k\right), \quad \mathbf{K} = k\mathring{\boldsymbol{\kappa}}_j. \tag{A.7}$$

We rewrite (A.7) as

$$\begin{aligned}&\hat{\bar{u}}^b_j\left(\mathbf{K} + k\mathring{\boldsymbol{\kappa}}^i, \omega\right) \\ &\qquad = i\pi k\bar{O}(\mathbf{K})\delta\left(|\mathbf{K} + k\mathring{\boldsymbol{\kappa}}^i| - k\right), \quad K_z \lessgtr -k\zeta^i\end{aligned} \tag{A.8}$$

where the last condition applies to $j = 1, 2$, respectively, implying that $\hat{\bar{u}}^b_j$ corresponds to the dashed and the solid-line hemispheres in Fig. §§2.

C. Proof of (2) and (3)

The K-space representation of the imaging field, defined in (2), is obtained by substituting (A.1)

$$\hat{\hat{I}}_j(\mathbf{K},\omega)=\frac{i}{v_0k^2}\left(\mathring{\boldsymbol{\kappa}}^i\cdot\mathbf{K}\right)\hat{\hat{u}}_j^b\left(\mathbf{K}+k\mathring{\boldsymbol{\kappa}}^i\right)\delta\left(|\mathbf{K}+k\mathring{\boldsymbol{\kappa}}^i|-k\right),\quad K_z\lessgtr-k\zeta^i,\quad k>0. \tag{A.9}$$

Substituting the weak scattering model (A.8), we obtain

$$\hat{\hat{I}}_j(\mathbf{K},\omega)=\frac{-\pi}{\omega}\left(\mathring{\boldsymbol{\kappa}}^i\cdot\mathbf{K}\right)\bar{O}(\mathbf{K})\,\delta\left(|\mathbf{K}+k\boldsymbol{\kappa}^i|-k\right),\quad K_z\lessgtr-k\zeta^i,\quad k>0. \tag{A.10}$$

Combining $\hat{\hat{I}}_1$ and $\hat{\hat{I}}_2$, we yield

$$\hat{\hat{I}}(\mathbf{K},\omega)=\frac{-\pi}{\omega}\left(\mathring{\boldsymbol{\kappa}}^i\cdot\mathbf{K}\right)\bar{O}(\mathbf{K})\delta\left(|\mathbf{K}+k\boldsymbol{\kappa}^i|-k\right),\quad k>0. \tag{A.11}$$

Next, we calculate the transient imaging field

$$\overset{+}{I}(\mathbf{r},t)=\frac{1}{\pi}\int_0^\infty d\omega\, e^{-i\omega t}I(\mathbf{r},\omega). \tag{A.12}$$

Inserting the weak scattering model for $\overset{+}{I}$ in (A.11), we obtain

$$\overset{+}{\bar{I}}(\mathbf{K},t)=-\int d\omega\, e^{-i\omega t}\frac{\mathring{\boldsymbol{\kappa}}^i\cdot\mathbf{K}}{\omega}\bar{O}(\mathbf{K})\,\delta\left(|\mathbf{K}+k\boldsymbol{\kappa}^i|-k\right). \tag{A.13}$$

For positive ω, the δ function can be expressed as

$$\begin{aligned}\delta\left(|\mathbf{K}+k\mathring{\boldsymbol{\kappa}}^i|-k\right)&=\delta\left(\sqrt{\left(K_x+k\xi^i\right)^2+\left(K_z+k\zeta^i\right)^2}-k\right)\\&=\frac{v_0|\mathbf{K}|^2}{2\left(\mathring{\boldsymbol{\kappa}}^i\cdot\mathbf{K}\right)^2}\delta\left(\omega+v_0\frac{|\mathbf{K}|^2}{2\mathring{\boldsymbol{\kappa}}^i\cdot\mathbf{K}}\right)\end{aligned} \tag{A.14}$$

where we used $\mathring{\boldsymbol{\kappa}}^i$ from (§§3). Substituting (A.11) into (A.10), we find that

$$\overset{+}{\bar{I}}(\mathbf{K},t)\Big|_{t=0}=\bar{O}(\mathbf{K}). \tag{A.15}$$

Equation (A.15) applies only for $\mathbf{K}$ in the left-hand side $K_z<0$ of the K-space. Since O is real, the value of $\bar{O}$ on the right-hand side is symmetric. It follows that:

$$\mathrm{Re}\,\overset{+}{I}_j(\mathbf{r},t)\big|_{t=0}=2O(\mathbf{r}) \tag{A.16}$$

which is our final result.

Appendix B
Derivation of (11)

The imaging fields are given by (2). Substituting their spectral representation [see (1)], they are given by

$$\hat{I}_j(\mathbf{r},\omega)=v_0^{-1}k^{-2}\times\mathring{\boldsymbol{\kappa}}^i\cdot\nabla\left[e^{-ik\mathring{\boldsymbol{\kappa}}^i\cdot\mathbf{r}}\left(\frac{k}{2\pi}\right)^2\int_{\mathcal{P}}d^2\xi\,\hat{\tilde{u}}_j(\boldsymbol{\xi})\,e^{ik(\boldsymbol{\xi}\cdot\mathbf{x}\mp\zeta z)}\right]. \tag{B.1}$$

Next, we use the BF representation of $\hat{\tilde{u}}_j(\boldsymbol{\xi})$. By using (9) and changing the order of integration and differentiation, we obtain

$$\hat{I}_j(\mathbf{r},\omega)=(i\omega)^{-1}e^{-ik\mathring{\boldsymbol{\kappa}}^i\cdot\mathbf{r}}\sum_{\boldsymbol{\mu}}\hat{A}^j_{\boldsymbol{\mu}}\times\left(\frac{k}{2\pi}\right)^2\int d^2\xi\left(1-\mathring{\boldsymbol{\kappa}}_j\cdot\mathring{\boldsymbol{\kappa}}^i\right)\hat{\tilde{\psi}}_{\boldsymbol{\mu}}(\boldsymbol{\xi})\,e^{\mp ik\zeta z}e^{ik\boldsymbol{\xi}\cdot\mathbf{x}}. \tag{B.2}$$

Finally, by evaluating the integral asymptotically and using the well-collimated approximation as in (§§9), i.e., $(\boldsymbol{\xi},\ \zeta)\simeq(\boldsymbol{\xi}_{\mathbf{n}},\ \zeta_{\mathbf{n}})$, we end up with the final result of (11).

Appendix C
Closed-Form Expression for the Scattered Field in the Born Approximation

To clarify the system's performance, we have explored in Figs. 3 and 7 the imaging using Born-approximated data that can be calculated in a closed form using (§§7), where $\bar{O}(\mathbf{K})$ corresponding to $O(\mathbf{r})$ of (§§35) is given by

$$\bar{O}(\mathbf{K})=2\pi\sum_l O_l\sigma_{1_l}\sigma_{2_l}e^{-\frac{1}{2}\left(K_1^2\sigma_{1_l}^2+K_2^2\sigma_{2_l}^2\right)-i(K_xx_l+K_zz_l)} \tag{C.1}$$

where the parameters $(\sigma_{1_l},\sigma_{2_l})$ and (x_l,z_l) define the width and the centers of the l-Gaussian in (§§35), while (K_1,K_2) are the spectral parameters associated with (η_1,η_2) in (§§36) and are related to the global spectral parameters (K_x,K_z) via

$$\begin{pmatrix}K_1\\K_2\end{pmatrix}=\begin{pmatrix}\cos\theta_l&-\sin\theta_l\\\sin\theta_l&\cos\theta_l\end{pmatrix}\begin{pmatrix}K_x\\K_z\end{pmatrix} \tag{C.2}$$

with θ_l denoting the rotation of the Gaussians. The specific parameters taken are listed in Table §§I.

References

[1] R. Tuvi, E. Heyman, and T. Melamed, "UWB beam-based local diffraction tomography—Part I: Phase-space processing and physical interpretation," *IEEE Trans. Antennas Propag.*, vol. 68, no. 10, pp. 7144–7157, Oct. 2020.

[2] R. Tuvi, E. Heyman, and T. Melamed, "Beam frame representation for ultrawideband radiation from volume source distributions: Frequency-domain and time-domain formulations," *IEEE Trans. Antennas Propag.*, vol. 67, no. 2, pp. 1010–1024, Feb. 2019.

[3] T. Melamed, Y. Ehrlich, and E. Heyman, "Short-pulse inversion of inhomogeneous media: A time-domain diffraction tomography," *Inverse Problems*, vol. 12, no. 6, pp. 977–993, Dec. 1996.

[4] K. J. Langenberg, "Applied inverse problems for acoustic, electromagnetic and elastic wave scattering," in *Basic Methods of Tomography and Inverse Problems* (Malvern Physics Series), P. C. Sabatier, Ed. Bristol, U.K.: Adam Hilger, 1987.

[5] A. J. Devaney, *Mathematical Foundations of Imaging, Tomography and Wavefield Inversion*. Cambridge, U.K.: Cambridge Univ. Press, 2012.

[6] T. Heilpern, A. Shlivinski, and E. Heyman, "Back-propagation and correlation imaging using phase-space Gaussian-beams processing," *IEEE Trans. Antennas Propag.*, vol. 61, no. 11, pp. 5676–5688, Nov. 2013.

[7] T. Heilpern and E. Heyman, "MUSIC imaging using phase-space Gaussian-beams processing," *IEEE Trans. Antennas Propag.*, vol. 62, no. 3, pp. 1270–1281, Mar. 2014.

[8] W. C. Chew and Y. M. Wang, "Reconstruction of two-dimensional permittivity distribution using the distorted born iterative method," *IEEE Trans. Med. Imag.*, vol. 9, no. 2, pp. 218–225, Jun. 1990.

[9] R. Tuvi, Z. Zhao, and M. K. Sen, "Multi frequency beam-based migration in inhomogeneous media, using windowed Fourier transform frames," *Geophys. J. Int.*, accepted for publication.

Ram Tuvi was born in Holon, Israel, in 1982. He received the B.Sc. and M.Sc. degrees *(cum laude)* in electrical and computer engineering from the Ben-Gurion University of the Negev, Beersheba, Israel, in 2010 and 2013, respectively, and the Ph.D. degree from the School of Electrical Engineering, Tel Aviv University, Tel Aviv, Israel, in 2019.

He is currently a Post-Doctoral Fellow with the group of Prof. M. K. Sen at the Institute for Geophysics, University of Texas at Austin, Austin, TX, USA. His research interests include electromagnetics and geophysics, analytical and numerical techniques in wave theory, scattering, and inverse scattering.

Ehud Heyman (Life Fellow, IEEE) was born in Tel Aviv, Israel, in 1952. He received the B.Sc. degree *(summa cum laude, Valedictorian)* in electrical engineering from Tel Aviv University, Tel Aviv, in 1977, the M.Sc. degree (Hons.) in electrical engineering from the Technion–Israel Institute of Technology, Haifa, Israel, in 1979, and the Ph.D. degree in electro-physics from the Polytechnic Institute of New York, New York, NY, USA, in 1982.

While at the Polytechnic Institute of New York, he was a Rothschild Fellow, a Fullbright Fellow, and a Hebrew Technical Institute Fellow. In 1983, he joined the Department of Physical Electronics, Tel Aviv University, where he is currently a Professor and the incumbent of the Jokel Chair of Electromagnetics. He served as the Department Head, the Founding Head of the School of Electrical Engineering from 2002 to 2005, and the Dean of Engineering from 2005 to 2014. He published over 120 refereed journal articles, and was an invited speaker at many international conferences. His research interests involve analytic methods in wave theory, including asymptotic and time-domain techniques for propagation and scattering, beam and pulsed-beam techniques, short-pulse antennas, inverse scattering, target identification, imaging and synthetic aperture radar, and propagation in a random medium.

Dr. Heyman is a fellow of the IEEE Antennas and Propagation Society, a member of Sigma Xi, and the Chairman of the Israeli National Committee for Radio Sciences (URSI). He was a recipient of the Balthasar van der Pol Gold Medal Award of URSI for the year 2011. He was an Associate Editor of the IEEE Press Series on Electromagnetic Waves and the IEEE TRANSACTIONS ON ANTENNAS AND PROPAGATION.

Timor Melamed (Senior Member, IEEE) was born in Tel Aviv, Israel, in January 1964. He received the B.Sc. degree *(magna cum laude)* in electrical engineering and the Ph.D. degree from Tel Aviv University, Tel Aviv, in 1989 and 1996, respectively.

From 1996 to 1998, he held a post-doctoral position at the Department of Aerospace and Mechanical Engineering, Boston University, Boston, MA, USA, and collaborated with Prof. L. B. Felsen. He is currently with the School of Electrical and Computer Engineering, Ben-Gurion University of the Negev, Be'er Sheva, Israel. His main fields of interest include propagation and scattering of waves, analytical methods in the time domain, scattering from moving objects, and beam methods.